PROCEEDINGS OF THE ROYAL SOCIETY A

Proc. R. Soc. A (2009) **465**, 915–935
doi:10.1098/rspa.2008.0342
Published online 4 December 2008

A constant shear stress core flow model of the bidirectional vortex

By Brian A. Maicke and Joseph Majdalani*

University of Tennessee Space Institute, Tullahoma, TN 37388, USA

In this paper, we discuss the merits of two models for the swirl velocity in the core of a confined bidirectional vortex. The first is piecewise, Rankine-like, based on a combined-vortex representation. It stems from the notion that a uniform shear stress distribution may be assumed in the inner vortex region of a cyclone, especially at high Reynolds numbers. Thereafter, direct integration of the shear stress enables us to retrieve an expression for the swirl velocity that overcomes the inviscid singularity at the centreline. The second model consists of a modified asymptotic solution to the problem obtained directly from the Navier–Stokes equations. Both solutions we present transition smoothly to the outer, free-vortex approximation at some intermediate position in the chamber. This position is deduced from available experimental data to the extent of providing an accurate swirl velocity distribution throughout the chamber. By scaling the constant shear radius to the core layer thickness, the constant of proportionality is readily calculated using the method of least squares. Interestingly, the constant of proportionality is found to be invariant at several vortex Reynolds numbers, thus helping to achieve closure. The combined-vortex representation is validated against a large body of experimental measurements and through comparisons to a laminar core model that is enhanced through the use of an eddy viscosity. Other heuristic schemes are discussed and the two most suitable models to capture realistic flow behaviour at high vortex Reynolds numbers are identified. Our two models are first derived analytically and then anchored on the available experimental measurements.

Keywords: rotating; cyclonic; confined bidirectional vortex; two-cell bipolar; centrifugal separator; high speed Rankine flow

1. Introduction

From the pioneering days of Rankine (1858) to the present era, swirling flows have remained the subject of ceaseless scientific enquiry both owing to their interesting theoretical challenges and their effective usage in industrial applications. Historically, the earliest theoretical models have been fundamentally connected with unbounded geophysical flows that spontaneously occur in nature. In this vein, hurricanes and tornadoes have been sporadically modelled using a variety of vortex flow fields (see Penner 1972). Even stellar phenomena

* Author and address for correspondence: Department of Mechanical, Aerospace and Biomedical Engineering, University of Tennessee Space Institute, 411 B. H. Goethert Parkway, Tullahoma, TN 37388, USA (maji@utsi.edu).

Received 18 August 2008
Accepted 31 October 2008

have been subjected to similar exploratory lines of enquiry (Königl 1986). While large-scale vortex patterns have constituted the motivation for much of the earlier work, modern investigations have constantly strived to harness the power of swirl in emerging products and mechanical equipment, both domestic and commercial. One may also classify applications into those that employ unidirectional swirl (e.g. swirl combustors) and those that rely on a more complex, self-reversing motion often termed bidirectional.

In the context of wall-bounded bidirectional swirl, one may cite the work of ter Linden (1949) that has focused on studying the efficiency of cyclone separators. Later, Bloor & Ingham (1987) have analysed the incompressible fluid motion in a conical cyclone using spherical coordinates. More recently, Vyas *et al.* (2003), Vyas & Majdalani (2006*a*,*b*), Batterson & Majdalani (2007) and Majdalani & Rienstra (2007) have developed both exact and asymptotic solutions to describe bidirectional flow motions in cylindrical and spherical geometries. Their work has been motivated by a propulsive application, specifically by the need to extend the understanding of gaseous motions in the vortex combustion cold-wall chamber developed by Chiaverini *et al.* (2003).

Even with a continually renewed interest in cyclonic flows, especially of the confined type, one can note a dearth of rigorous analytical models to describe these flow fields (Vatistas *et al.* 2005). Given that strictly inviscid solutions regularly capture most essential features of swirl, more elaborate models are often deemed either intractable or unnecessary. It may thus be argued that while inviscid solutions may be appropriate for unbounded, swirling flows, they can fail to capture the physics of confined motions. When the flow field is surrounded by solid boundaries, the effects of no slip at the walls and singularities at the core can significantly alter the bulk motion. In practice, the characteristics of the core are relatively well understood and have been described by Ogawa (1984), Vatistas *et al.* (1986), Hoekstra *et al.* (1998) and more recently by Derksen & Van den Akker (2000), Fang *et al.* (2003), Rom *et al.* (2004), Murray *et al.* (2004) and Hu *et al.* (2005). Nonetheless, a rigorous analytical model for the core is still lacking, especially at high Reynolds numbers. Another reason that new models for confined vortex flows are scant may be linked to the complexity of their governing equations. Given this perspective, Vyas & Majdalani (2006*a*,*b*) have pursued the development of an exact inviscid model, followed by a laminar boundary layer model to capture the effects of viscosity on the tangential velocity in the bidirectional vortex chamber. Along similar lines, Batterson & Majdalani (2007) have extended the viscous analysis to account for axial and radial boundary layers. These solutions have not only furthered our understanding of the flow field but have also opened up new lines of research enquiries.

Realizing that the existing solutions stem from fundamental equations that govern laminar flow motion, it may be useful to follow tradition and employ them as a springboard for developing approximations for turbulent flows. At first, this paradigm may be perhaps counterintuitive, as turbulence is unsteady, random and three-dimensional in nature, all of which are being contrary to the conditions employed here. However, experimental observation has repeatedly shown that the core of the confined vortex is nearly laminar in behaviour (Escudier *et al.* 1982; Derksen 2005). This widely accepted hypothesis inspires us to explore a core model based on the constant shear stress that one would expect in the low turbulence region at the centre of the chamber. With this in mind, it is

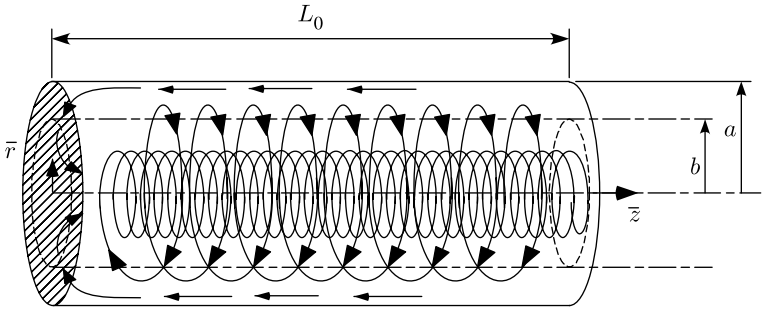

Figure 1. Geometric characteristics of the bidirectional vortex chamber.

the goal of this study to present an alternative swirl velocity model that approximates the turbulent core behaviour in a bidirectional vortex chamber. A combined-vortex, Rankine-type matching radius is then specified to grant the model some freedom in reproducing the essential features of a swirl-dominated motion. Two fundamental examples of the matching technique are explored. In the first, the constant shear stress representation is compared with the asymptotic solution of Vyas *et al.* (2003) obtained in the presence of a viscous core boundary layer. This comparison enables us to verify that the alternate model provides a suitable theoretical basis for capturing the fundamental characteristics of the flow. In the second, the theoretical model is anchored based on experimental data obtained by Rom (2006) at high vortex Reynolds numbers. Finally, the validity of the resulting models is discussed and an outlook towards future research is presented.

2. Mathematical model

(*a*) *Geometry*

This work focuses on the swirl velocity of an axisymmetric, incompressible, steady, rotational flow spiralling inside a cylindrical chamber of length L_0 and radius a. The origin of the coordinate system is fixed at the centre of the inert headwall, and a partially open downstream end is taken to have a radius b (figure 1). The radial and axial directions are denoted by $\bar{r}$ and $\bar{z}$, respectively. A single phase, non-chemically reactive fluid is injected at the base of the chamber, at $\bar{r}=a$, in a purely tangential manner and at an average circumferential velocity of $\bar{u}_\theta = U$. Owing to wall collisions and subsequent bending, the tangentially injected fluid quickly develops axial motion that follows a helical path up to the headwall. The flow then reverses axial direction and spirals down the centre of the chamber, thus exiting at $\bar{z}=L_0$. The attendant geometric parameters consist of the fraction of radius open at the base, defined as $\beta = b/a$, and the aspect ratio of the chamber, given by $L = L_0/a$.

(*b*) *Basic formulation*

The formulation follows precisely that presented by Vyas & Majdalani (2006*a*). For the reader's convenience, the normalized governing equations are reproduced here, assuming axisymmetric conditions and an axially invariant

swirl velocity as

$$u_r \frac{\partial u_r}{\partial r} + u_z \frac{\partial u_r}{\partial z} - \frac{u_\theta^2}{r} = -\frac{\partial p}{\partial r}, \tag{2.1}$$

$$u_r \left(\frac{\partial u_\theta}{\partial r} + \frac{u_\theta}{r} \right) = 0, \tag{2.2}$$

$$u_r \frac{\partial u_z}{\partial r} + u_z \frac{\partial u_z}{\partial z} = -\frac{\partial p}{\partial z}, \tag{2.3}$$

where

$$\begin{cases} z = \dfrac{\bar{z}}{a}, \qquad r = \dfrac{\bar{r}}{a}, \qquad \nabla = a\bar{\nabla}, \qquad \beta = \dfrac{b}{a}, \qquad p = \dfrac{\bar{p}}{\rho U^2} \\ u_r = \dfrac{\bar{u}_r}{U}, \qquad u_\theta = \dfrac{\bar{u}_\theta}{U}, \qquad u_z = \dfrac{\bar{u}_z}{U}, \qquad Q_i = \dfrac{\bar{Q}_i}{Ua^2}. \end{cases} \tag{2.4}$$

Here $\bar{Q}_i$ is the volumetric flow rate at the inlet and A_i is the inlet area. We define the Stokes stream function as

$$u_r = -\frac{1}{r}\frac{\partial \psi}{\partial z}, \qquad u_z = \frac{1}{r}\frac{\partial \psi}{\partial r}. \tag{2.5}$$

Given steady inviscid conditions, one may relate the azimuthal vorticity to the stream function using $\Omega_\theta = C^2 r \psi$. When coupled with (2.5), this relation allows us to satisfy the vorticity transport equation while transforming the vorticity equation into

$$\frac{\partial^2 \psi}{\partial r^2} - \frac{1}{r}\frac{\partial \psi}{\partial r} + \frac{\partial^2 \psi}{\partial z^2} + C^2 r^2 \psi = 0. \tag{2.6}$$

Following Leibovich (1978), Bloor & Ingham (1987) and Szeri & Holmes (1988), the swirl velocity may be assumed to be independent of both axial and azimuthal variations. At the outset, (2.2) decouples from the other velocity terms. This enables us to employ the stream function-vorticity relation, given by (2.6), and subject to the following boundary conditions

$$\left.\begin{array}{lll} \bar{r} = a, \quad \bar{z} = L_0, \quad \bar{u}_\theta = U & & \text{circumferential velocity at entry} \\ \bar{r} = a, \quad \bar{z} < L_0, \quad \bar{u}_\theta = 0 & & \text{no slip condition at the sidewall} \\ \bar{r} = 0, \quad \forall\, \bar{z}, \quad \bar{u}_\theta = 0 & & \text{forced vortex center} \\ \bar{z} = 0, \quad \forall\, \bar{r}, \quad \bar{u}_z = 0 & & \text{impervious headwall} \\ \bar{r} = 0, \quad \forall\, \bar{z}, \quad \bar{u}_r = 0 & & \text{no flow across centreline} \\ \bar{r} = a, \quad \forall\, \bar{z}, \quad \bar{u}_r = 0 & & \text{impervious sidewall} \\ \int_b^a \bar{u}_z(\bar{r}, L_0)\bar{r}\, \mathrm{d}\bar{r} = \bar{Q}_i & & \text{axial inflow matching tangential source.} \end{array}\right\} \tag{2.7}$$

The (r, z) versus θ segregation allows us to introduce a swirl velocity model after Vyas & Majdalani (2006*a*). Their exact inviscid solution is simply

$$\left.\begin{aligned} \boldsymbol{u} &= -\kappa\frac{\sin(\pi r^2)}{r}\,\boldsymbol{e}_r + \frac{1}{r}\,\boldsymbol{e}_\theta + 2\pi\kappa z\cos(\pi r^2)\boldsymbol{e}_z, \\ \Delta p &= -\frac{1}{2r^2}\left\{1+\frac{1}{2}\kappa^2\left[8\pi^2 r^2 z^2 + 1 - \cos(2\pi r^2)\right]\right\}, \end{aligned}\right\} \tag{2.8}$$

where the geometric inflow parameter is defined as $\kappa = Q_i/(2\pi L)$ The corresponding quasi-viscous solution that captures the forced vortex near the core has also been derived by Vyas & Majdalani (2006*b*). It can be written as

$$\left.\begin{aligned} \boldsymbol{u} &= -\kappa\frac{\sin(\pi r^2)}{r}\,\boldsymbol{e}_r + \frac{1}{r}(1-e^{-Vr^2/4})\boldsymbol{e}_\theta + 2\pi\kappa z\cos(\pi r^2)\boldsymbol{e}_z, \\ \Delta p &= -\frac{1}{2r^2}\left\{\begin{aligned} &1+\frac{1}{2}\kappa^2\left[8\pi^2 r^2 z^2 + 1 - \cos(2\pi r^2)\right] + e^{-Vr^2/2} - 2e^{-Vr^2/4} \\ &+\frac{1}{2}r^2 V\left[\mathrm{Ei}\left(-\frac{1}{2}Vr^2\right) - \mathrm{Ei}\left(-\frac{1}{4}Vr^2\right)\right] \end{aligned}\right\}, \end{aligned}\right\} \tag{2.9}$$

where the vortex Reynolds number is given by

$$V = \frac{Re}{\sigma}\,\frac{a}{L_0} = \frac{\bar{Q}_i}{L_0\nu}. \tag{2.10}$$

Note that $\sigma = a^2/A_i$ constitutes a modified form of the swirl number introduced by Gupta *et al.* (1984), namely, $S = \pi ab/A_i = \pi\beta a^2/A_i = \pi\beta\sigma$. In the remainder of this study, (2.9) will be referred to as the laminar core model.

3. Constant shear-stress model

The free vortex motion in the outer domain is dictated by the inviscid solution given by (2.8). Our main focus is directed to the inner region, specifically to the development of a model that can capture the behaviour of the flow in the core vortex at high Reynolds numbers. We require the model to remain consistent with the outer motion, merging smoothly with the outer vortex without becoming unbounded at the centreline. Since the flow under high speed conditions can deviate from the inviscid representation, one must tread carefully in conceiving a suitable model. Following Townsend (1976) or Tennekes & Lumley (1976), one can put

$$(\boldsymbol{u}\cdot\nabla)\boldsymbol{u} = -\nabla p + \nabla\cdot\boldsymbol{\tau}. \tag{3.1}$$

For fully developed motion in the tangential direction, it follows that an equilibrium may be maintained between shear and pressure terms under either laminar or turbulent conditions. Then considering a flow with a zero tangential pressure gradient, the dominant shear stress in the tangential direction may be

assumed to be spatially uniform. This enables us to set

$$\tau_{r\theta} = \varepsilon\left[\frac{1}{r}\frac{\partial u_r}{\partial \theta} + r\frac{\partial}{\partial r}\left(\frac{u_\theta}{r}\right)\right] = \varepsilon r\frac{\partial}{\partial r}\left(\frac{u_\theta}{r}\right) = C_1, \tag{3.2}$$

where the viscous parameter ε is small, being inversely proportional to the Reynolds number

$$\varepsilon \equiv \frac{1}{Re} = \frac{\nu}{Ua}. \tag{3.3}$$

The forced vortex solution, for which vorticity is uniformly distributed in the core region, $u_\theta \propto r$, may be restored from (3.2) by setting $C_1 = 0$. To obtain a more general expression, we assume a constant shear in the core region (Tennekes & Lumley 1976; Townsend 1976; White 1991). We then integrate (3.2) to obtain

$$u_\theta^{(\mathrm{i})} = r\left[\frac{C_1}{\varepsilon}\ln(r) + C_2\right]. \tag{3.4}$$

It may be interesting to note that each of the two undetermined constants, C_1 and C_2, have a clear physical meaning: while the first relates to the swirl strength of the velocity component generating the stress, the second corresponds to the swirl strength of a flow undergoing solid body rotation. Here, the superscript (i) denotes a solution in the inner region. The two undetermined constants can be manipulated to match the inner solution with the outer, free vortex expression at their intersection point. This is achieved by equating the velocity and its derivative to the outer vortex at a specific matching radius. Since the matching radius is not known *a priori*, it must be carefully specified. For the moment, we solve for a yet to be determined matching point $X = f(V)$, where X is an unspecified location written as a function of the vortex Reynolds number. At the outset, (3.4) may be expressed as

$$u_\theta = \begin{cases} \dfrac{r}{X^2}\left[1 - \ln\left(\dfrac{r^2}{X^2}\right)\right]; & r \le X \\ \dfrac{1}{r}; & r > X. \end{cases} \tag{3.5}$$

In what follows, this combined-vortex model is referred to as the constant shear model. The incontrovertible analogy with Rankine's laminar model is evident. Using our nomenclature, Rankine's combined vortex may be represented by

$$u_\theta = \begin{cases} r/X^2; & r \le X \\ 1/r; & r > X. \end{cases} \tag{3.6}$$

Here $X = U/\bar{u}_\theta(aX)$ is the point where the inner vortex line intersects with the sloping tail of the outer vortex. This location also defines Rankine's maximum swirl velocity $(\bar{u}_\theta)_{\max} = \bar{u}_\theta(aX)$. By contrast to the constant shear solution that predicts constant shear throughout the core region, Rankine's model predicts constant vorticity for $r \le X$.

Given that the inner core velocity is bounded at the centreline, a companion pressure may be obtained that does not exhibit the inviscid singularity of its predecessor (see Vyas & Majdalani 2006*a*). From (2.1) and (2.3), the axially and

radially integrated pressures become

$$p-p(1,0)=-\int_1^r\left(u_r\frac{\partial u_r}{\partial \bar{r}}+u_z\frac{\partial u_r}{\partial z}-\frac{u_\theta^2}{r}\right)\mathrm{d}r \quad \text{and}$$
$$p-p(1,0)=-\int_0^z\left(u_r\frac{\partial u_z}{\partial \bar{r}}+u_z\frac{\partial u_z}{\partial z}\right)\mathrm{d}z. \tag{3.7}$$

Integration and combination of these equations provides the pressure distribution

$$\Delta p=\begin{cases}\dfrac{1}{2\kappa^4 r^2}\left(r^4\left\{5+\ln\left(\dfrac{r^4}{X^4}\right)\left[\ln\left(\dfrac{r}{X}\right)-2\right]\right\}-\kappa^2X^4\sin^2(\pi r^2)\right)\\ \quad -\kappa^2\left[4\pi^2z+\dfrac{\sin^2(\pi r^2)}{2r^2}\right]+K_1; & r\le X,\\ -\dfrac{1}{2r^2}[1+\kappa^2\sin^2(\pi r^2)]-\kappa^2\left[4\pi^2z+\dfrac{\sin^2(\pi r^2)}{2r^2}\right]+K_2; & r>X,\end{cases} \tag{3.8}$$

where $\Delta p=p-p(1,0)$. The constant K_1 is determined by setting the piecewise parts equal at $r=X$, while K_2 is calculated by securing the boundary condition at the outer radius of the headwall

$$\left.\begin{aligned}p(1,0)&=-\frac{1}{2}+K_2=0,\\ p(X,0)&=K_1+3X^{-2}=K_2,\end{aligned}\right\}\quad\text{or}\quad\left.\begin{aligned}K_1&=\frac{1}{2}-3X^{-2},\\ K_2&=\frac{1}{2}.\end{aligned}\right\} \tag{3.9}$$

We hence extract the piecewise distribution

$$\Delta p=\begin{cases}\dfrac{1}{2}-\dfrac{3}{X^2}-\kappa^2\left[4\pi^2z+\dfrac{\sin^2(\pi r^2)}{2r^2}\right]\\ \quad+\dfrac{1}{2\kappa^4r^2}\left(r^4\left\{5+\ln\left(\dfrac{r^4}{X^4}\right)\left[\ln\left(\dfrac{r}{X}\right)-2\right]\right\}-\kappa^2X^4\sin^2(\pi r^2)\right); & r\le X,\\ \dfrac{1}{2}-\dfrac{1}{2r^2}[1+\kappa^2\sin^2(\pi r^2)]-\kappa^2\left[4\pi^2z+\dfrac{\sin^2(\pi r^2)}{2r^2}\right]; & r>X.\end{cases} \tag{3.10}$$

4. Discussion

(a) *Laminar core model*

To illustrate the ability of the constant shear solution to embody different patterns, we start by reproducing the laminar core boundary layer model derived by Vyas & Majdalani (2006*b*). Clearly, if we are to claim a portable solution, the swirl velocity calculated from the present work must approximate key features

connected with the boundary layer model. For a simple demonstration of the matching paradigm, we implement the notion that swirl velocities from the laminar and constant shear models must exhibit the same maxima. This enables us to compare the principal flow attributes and gain insight into how the matching radius varies with the vortex Reynolds number.

While the inner part of the piecewise velocity yields

$$\left.\frac{\mathrm{d}u_\theta}{\mathrm{d}r}\right|_{r=r_{\max}} = 0 \quad \text{or} \quad r_{\max} = \frac{X}{\sqrt{e}}, \tag{4.1}$$

the laminar model projects

$$r_{\max} = \sqrt{\frac{2}{V}\left[-1-2\mathrm{pln}\left(-1,-\frac{1}{2}\,e^{-1/2}\right)\right]} \simeq \frac{2.242}{\sqrt{V}}. \tag{4.2}$$

These positions can be substituted back into their respective equations and then equated identically. One gets

$$\frac{2}{Xe^{1/2}} = 1-\exp\left[\frac{1}{2}+\mathrm{pln}\left(-1,-\frac{1}{2}\,e^{-1/2}\right)\right]\sqrt{\frac{-V}{2\left[1+2\mathrm{pln}\left(-1,-\frac{1}{2}\,e^{-1/2}\right)\right]}}. \tag{4.3}$$

Equation (4.3) enables us to solve for X as a function of V directly from

$$X = \frac{2}{\sqrt{eV}}\,\frac{\sqrt{-2\left[1+2\mathrm{pln}\left(-1,-\frac{1}{2}\,e^{-1/2}\right)\right]}}{\left\{1-\exp\left[\frac{1}{2}+\mathrm{pln}\left(-1,-\frac{1}{2}\,e^{-1/2}\right)\right]\right\}} \simeq \frac{3.802}{\sqrt{V}}. \tag{4.4}$$

This matching radius X permits our piecewise velocity to capture the same peak velocity that the laminar boundary-layer solution projects as a function of V.

A comparison of the different swirl velocity models at three increasing vortex Reynolds numbers is presented in figure 2. While the free vortex is invariant with respect to V, both the present study and the laminar boundary layer model capture the increasing velocity peaks and their translation towards the centreline with successive increases in V. Note that the two models match identically at the point of the highest velocity, owing to the imposed matching treatment. They also behave rather similarly elsewhere in the domain, with the constant shear model decreasing from the peak velocity more slowly, owing to its wider profile. This behaviour is consistent with observations of turbulent vortices.

Figure 3 compares the pressure distributions of the two models at two vortex Reynolds numbers. The radial pressure gradient in figure 3*a* is slightly higher in the case of the constant shear model, especially in the core region. This behaviour can be accounted for by the slightly increased velocity anticipated from the piecewise model near the centreline. Except for these differences, the piecewise model seems to faithfully capture the general shape of the radial pressure distribution. The actual pressure drop is shown in figure 3*b*. The constant shear pressure starts slightly higher, but then quickly diminishes to match the laminar core approximation. It should be noted that the constant shear solution offers one degree of freedom that can be adjusted to suit a particular application. For example, should accurate prediction of the pressure stand as the most valuable requirement for a specific situation, then the matching radius could be adjusted to best fit the experimental pressure data near the core. A similar paradigm is

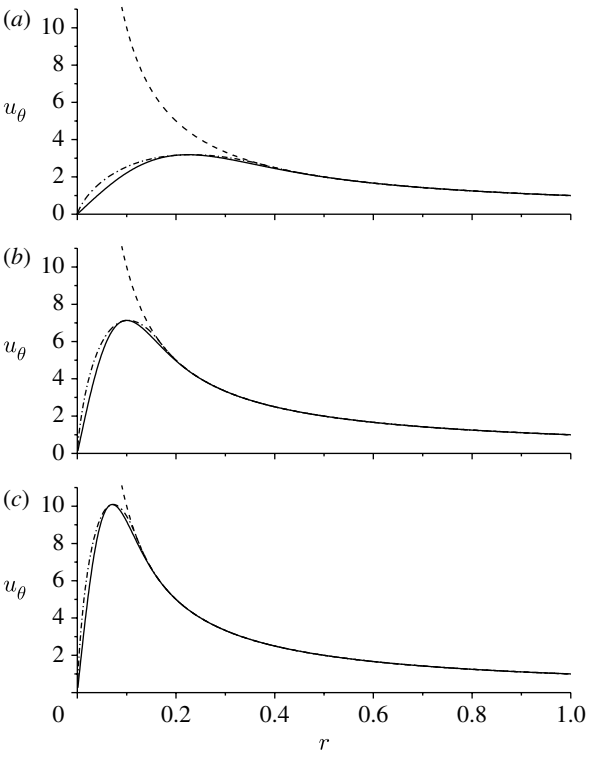

Figure 2. (*a*) Comparison at $V=100$, (*b*) 500, and (*c*) 1000. Solid line, laminar core; dashed-dotted line, constant shear; dashed line, free outer vortex. Note the constant shear stress model nearly duplicating the laminar solution for a matching radius of $X=3.802/\sqrt{V}$.

used in modelling large atmospheric flows where only pressure-related measurements may be available (Trapp 2000). As affirmed by Alekseenko *et al.* (1999), the swirl velocity core may be reconstructed in the absence of vortex breakdown using pressure measurements alone.

Before concluding this comparison, it may be instructive to examine the behaviour of shear and vorticity near the axis of rotation. In the view of the shear stress being a quintessential contributor in the derivation of the constant shear approximation, we compare the present result to the laminar core solution by Vyas *et al.* (2003). The latter is given by

$$\tau_{r\theta} = -2\varepsilon r^{-2}\left[1-\left(1+\frac{1}{4}r^2 V\right)e^{-Vr^2/4}\right]. \tag{4.5}$$

Since only amendments to the swirl velocity are considered here, the affected member of the shear stress tensor is $\tau_{r\theta}$. Recalling the general form from (3.2), we find after substitution

$$\tau_{r\theta} = \varepsilon r\frac{\partial}{\partial r}\left(\frac{u_\theta}{r}\right) = \begin{cases} -\dfrac{2\varepsilon}{X^2}; & r \le X \\ -\dfrac{2\varepsilon}{r^2}; & r > X. \end{cases} \tag{4.6}$$

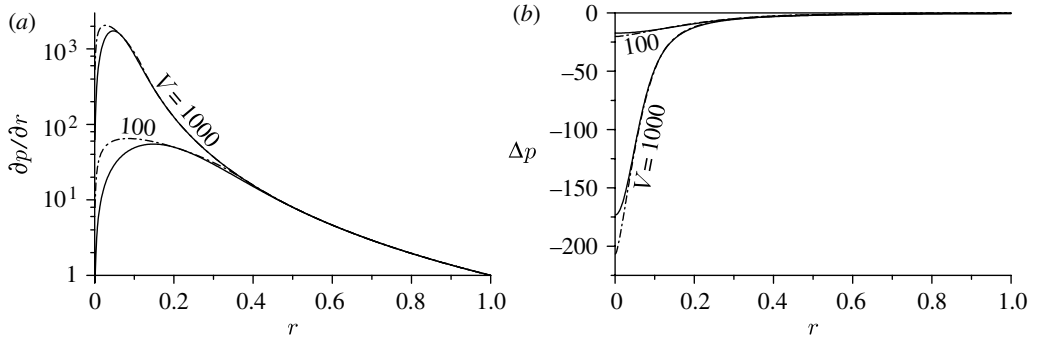

Figure 3. Comparison for (*a*) the radial pressure gradient and (*b*) the pressure distribution. Solid line, laminar core; dashed-dotted line, constant shear.

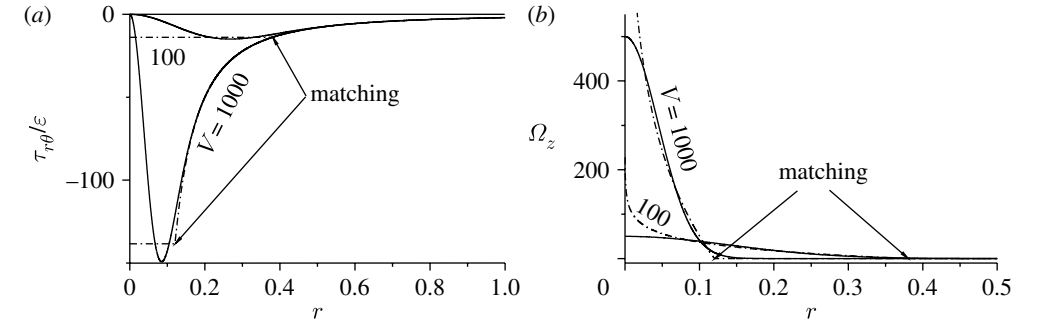

Figure 4. Comparison for (*a*) the shear stress and (*b*) the axial component of vorticity. Solid line, laminar core; dashed-dotted line, constant shear.

For the vorticity, we find

$$\Omega_z = \frac{1}{r}\frac{\partial(ru_\theta)}{\partial r} = \begin{cases} -\dfrac{4}{X^2}\ln\left(\dfrac{r}{X}\right); & r \le X \\ 0; & r > X. \end{cases} \tag{4.7}$$

The resultant curves are plotted in figure 4 and compared with the results of the laminar core treatment, namely, to $\Omega_z = \frac{1}{2}V\exp(-\frac{1}{4}Vr^2)$. In both parts of figure 4, we see that past the matching radius, a good agreement between the models is attained. Closer to the core, a deviation is manifested as a result of the constant shear stress model becoming uniform. As shown in figure 4*a*, the constant core value of the absolute shear $|\tau_{r\theta}|$ is slightly lower than the maximum laminar core value. Aside from this disparity near the centreline, the constant shear and laminar core curves are concurrent elsewhere in the domain. In figure 4*b*, the vorticity prescribed by the piecewise model is seen to mimic the laminar core curve. However, unlike the laminar model that smoothly tapers off in the vicinity of the core, the constant shear vorticity does not approach a constant as $r \to 0$.

By comparing the combined-vortex representation to the laminar core model, two key observations may be drawn. The first consists of the ability of the shear stress model to mimic the features seen in the laminar core without a viscous perturbation near the centreline. By avoiding such analysis, we no longer depend

on the existence of a first-order radial velocity and small parameter expansions. The outcome is a model that captures the core behaviour while requiring less overhead. The second benefit of a laminar core analogy is the development of a relation such as (4.4). This analytical expression linking the vortex Reynolds number to the matching radius X will later prove instrumental for properly interpreting experimental case studies.

(*b*) *Experimentally correlated model*

One of the chief attributes of the piecewise solution stems from its display of a single degree of freedom that can be adjusted to minimize the error in its prediction. For example, knowing that the laminar boundary layer treatment can over-predict the velocity distribution near the core when the flow is turbulent, an empirically based correction is necessary (e.g. when $V=10^4$ the laminar model predicts $(u_\theta)_{\max}=32$, an overestimated value). One avenue to evaluate this correction is through a least-squares analysis that enables us to determine the optimal matching radius that best fits experimental data. If a sufficient number of experiments are used, one could then deduce a relationship between the vortex Reynolds number and the matching location. Another possible approach is to introduce an effective vortex Reynolds number that can be correlated to its experimental counterpart. Given the increased turbulent viscosity at high speeds, the Reynolds number measured in laboratory tests could thus be converted into a smaller effective laminar equivalent that would be suitably retrofitted into the laminar solution. We explore both of these methods vis-à-vis the experimental data obtained by Rom (2006).

To set the stage, Rom's apparatus is equipped with particle image velocimetry (PIV) and a smoke generator that is capable of producing 0.2 μm seed particles. Particle images are captured by a LaVision Flowmaster 3 camera and cross-correlated to provide the swirl velocity at three axial locations in the cylindrical quartz chamber. To create different test cases, a modular chamber is used to alter the aspect ratio. Four tangentially located inlets in the base plate provide an injection method consistent with the boundary conditions outlined in (2.7). Given an operating pressure of 275 kPa for the chamber, variable inlets provide injection pressure drops that range from 10 to 30% of the chamber pressure. A summary of the conditions for each trial of the experiment are provided in table 1. A schematic of the experimental setup is illustrated in figure 5 and a complete description is provided by Rom (2006). While the constant shear model may be applicable to other experiments and numerical simulations, results available in the literature are seldom correlated with the vortex Reynolds number.

Using a modified least-squares method similar to that employed by Vatistas (2006) we analyse Rom's data and seek to determine the matching radius that minimizes the error between theory and experiment. Realizing that the radii calculated by this method vary with the vortex Reynolds number, we embed the dependence on V using a theoretically based relation similar in form to (4.4)

$$X=\frac{X_0}{\sqrt{V_t}}, \tag{4.8}$$

where V_t is the turbulent vortex Reynolds number based on the molecular viscosity μ. In (4.8) the matching radius X is connected to the vortex Reynolds number through a yet to be determined constant. Because X only appears in the

Table 1. Experimental parameters for six test cases.

parameter	case 1	case 2	case 3	case 4	case 5	case 6
injector pressure drop, $\Delta\bar{p}$ (kPa)	27.6	55.2	82.8	55.2	27.6	55.2
chamber aspect ratio, L	2.4	2.4	4.4	3.4	4.4	4.4
total injection area, A_i (m^2)	2.30×10^{-4}	1.57×10^{-4}	1.23×10^{-4}	1.57×10^{-4}	2.30×10^{-4}	1.57×10^{-4}
average injection speed, U ($m\cdot s^{-1}$)	68.73	77.72	89.61	88.78	74.81	88.31
modified swirl number, $\sigma=a^2/A_i$	2.81	4.10	5.26	4.10	2.81	4.10
inflow parameter, $\kappa=1/(2\pi\sigma L)$	0.0239	0.0164	0.0069	0.0114	0.0129	0.0088
vortex Reynolds number, $V=\dot{m}_i/(L_0\mu)$	47 150	36 540	30 160	29 150	27 650	22 370

core region ($r<X$), the optimization procedure focuses on the points inside the matching radius, especially that the error outside of this region is invariant with respect to X. This permits the least squares methodology to optimize the solution in the crucially important core region. We select from three of the available cases summarized in table 2. We also hold three cases in reserve, so that we can test the validity of the relationship in (4.8) with independent data. While each set of experimental cases exhibits a slightly different matching radius, the values for X_0 appear to be in relatively good agreement (i.e. 50.7, 49.6 and 49.0 for turbulent vortex Reynolds numbers of $V_t\backsimeq30$, 37 and 47×10^3, respectively). This agreement lends support to our foregoing assumptions and enables us to seek a weighted average of the values for X_0. We get

$$X=\frac{50.0}{\sqrt{V_t}}. \tag{4.9}$$

By the way of confirmation, the same constant, $X_0\backsimeq50$, is obtained when the method of least squares is applied to the entire collection of data, thus sweeping over the three cases simultaneously with the role of V_t being fully factored in.

We also compare a modified version of the laminar solution to both the experimental data and to the constant shear stress model. To this end, the laminar model is modified by an estimated turbulent eddy viscosity that reduces the experimental vortex Reynolds number to a value that conforms to the experimental data. Following Faler & Leibovich (1978) or Escudier *et al.* (1980), we introduce the eddy viscosity ratio

$$\ell_t=\frac{\mu_t}{\mu}=\frac{\nu_t}{\nu}. \tag{4.10}$$

This enables us to determine ℓ_t empirically from a standard least-squares analysis. As shown in table 2, we find for each V_t a corresponding value for ℓ_t. Then based on the same three cases and 879 points, minimizing the least-squares error yields

$$\ell_t=151.8 \quad \text{or} \quad V=\frac{V_t}{\ell_t}=\frac{\bar{Q}_i}{L_0\nu_t}=\frac{\dot{m}_i}{L_0\mu_t}. \tag{4.11}$$

Table 2. Least-squares parameters for the constant shear and laminar core models.

V_t	X_0	X (matching point)	$50/\sqrt{V_t}$	ℓ_t
47 150	49.04	0.243	0.230	150.3
36 540	49.63	0.267	0.262	154.1
30 160	50.67	0.314	0.288	151.0

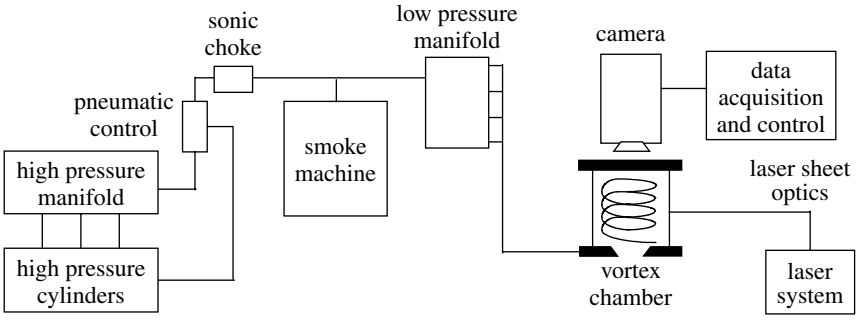

Figure 5. Schematic of experimental setup used by Rom (2006).

It is reassuring to note, within experimental uncertainty, the constancy of the eddy viscosity ratio over the range of Reynolds numbers considered. Physically, the adjustment in (4.11) leads to a vortex Reynolds number calculation based on the turbulent viscosity. Substitution into (2.9) enables us to express the modified laminar core solution in the form

$$\left.\begin{aligned} u_\theta &= \frac{1}{r}(1-e^{-Vr^2/4}),\\ \Delta p &= -\frac{1}{2r^2}\left\{\begin{aligned} &1+\frac{1}{2}\kappa^2[8\pi^2 r^2 z^2+1-\cos(2\pi r^2)],\\ &+e^{-Vr^2/2}-2e^{-Vr^2/4}+\frac{1}{2}Vr^2\left[\mathrm{Ei}\left(-\frac{1}{2}Vr^2\right)-\mathrm{Ei}\left(-\frac{1}{4}Vr^2\right)\right]. \end{aligned}\right\} \end{aligned}\right\} \tag{4.12}$$

To objectively compare the accuracy of the two models, we calculate several statistical parameters (table 3). By comparing correlation coefficients, r_{cc}, standard errors, σ_{e} and total relative errors, ΔE_{t}, the constant shear-based model seems to provide a slightly better fit to the data than the modified laminar distribution. The standard and total relative errors are calculated from

$$\sigma_{\mathrm{e}} = \frac{1}{\sqrt{n-1}}\sqrt{\sum_{i=1}^{n}[\hat{u}_\theta(r_i)-u_\theta(r_i)]^2} \quad \text{and}$$

$$\Delta E_{\mathrm{t}} = \sum_{i=1}^{n}[\hat{u}_\theta(r_i)-u_\theta(r_i)]^2 \Big/ \sum_{i=1}^{n}\hat{u}_\theta^2(r_i), \tag{4.13}$$

Table 3. Statistical characteristics of the constant shear and laminar core representations.

V_t	47 150			36 540			30 160		
	r_{cc}	σ_e	$\Delta E_t\%$	r_{cc}	σ_e	$\Delta E_t\%$	r_{cc}	σ_e	$\Delta E_t\%$
constant shear	0.900	0.558	4.36	0.968	0.253	1.23	0.880	0.376	3.19
laminar core	0.887	0.592	4.91	0.962	0.276	1.47	0.870	0.391	3.45

where n and $\hat{u}_\theta(r_i)$ denote the number of data points and the measured velocity at r_i, the radius of the ith data point. The standard error of the estimate quantifies the spread of data about the regression line, such as the standard deviation that measures the spread about a mean value. As shown in table 3, the total relative error falls under 3.2, 1.3 and 4.4% for the three cases associated with the constant shear approach. The corresponding experimental correlation coefficients are 0.88, 0.97 and 0.90, respectively. When the modified laminar core technique is used, the relative errors slightly increase to 3.5, 1.5 and 5.0%, with an equally minute reduction in r_{cc}.

Using (4.9) and (4.11), a comparison is drawn in figures 6 and 7 between the two empirical models and the experimental spread. The measurements collected in each trial case correspond to the data acquired at three axial locations in the vortex chamber, specifically at $z=0.2$, 0.5, and 0.7. On one hand, figures 6*a–c* display the collection of data that was used in the least squares analysis leading to the determination of the eddy viscosity ratio and the empirically based matching radius X. These three trials were selected for the fitting process owing to the relative fidelity of their data in the core region. On the other hand, figures 7*a–c* compare our solutions to the reserve datasets that were not used in the calculations, but rather saved for the sole purpose of testing the accuracy of these models at various Reynolds numbers. In both cases, the outer data follows quite faithfully the free vortex behaviour predicted by the outer solution. The agreement inside the core region is less appreciable. While both models capture the essential features of the data scatter, the constant shear-based model shows a broader bell-shaped contour than the narrower laminar profile. It is clear that as we approach the centreline, the experimental velocity begins to deviate from the maximum theoretical values projected by the analytical models. Of equal concern is the scatter and scarcity of data in the core region. Contrary to the large number of closely packed data points in the outer vortex region, fewer and more scattered data points appear near the core. This trend may be attributed to increased drag on seed particles in the high-speed region and to the natural tendency for separation of particles due to centrifugal entrainment. To overcome this problem, a different seeding method can be employed with a more elaborate experimental setup that correlates, for example, particle pairs from two pulsed laser planes. Additionally, strict control of the vortex Reynolds number for separate trial runs may increase the confidence in the measurements and corresponding matching-radius correlation. It may thus be speculated that data obtained from a more focused experiment could be higher and less noisy than the ones considered here.

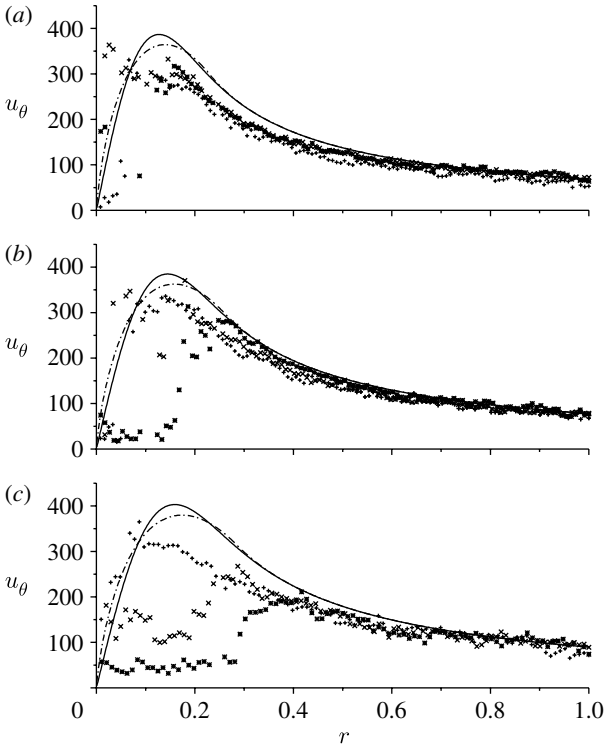

Figure 6. Comparison of the turbulent and modified laminar models with the experimental data used for the least squares analysis. Results are shown for (*a*) V_t=47 150, (*b*) 36 540, and (*c*) 30 160. Plus, z/L=0.2; cross, z/L=0.5; star, z/L=0.7.

Interestingly, the reduced fidelity in the vicinity of the core is also depicted in the Reynolds shear-stress model data and laser doppler velocimetry (LDV) measurements taken by Hu *et al.* (2005). Their LDV data acquisition system also deteriorates inwardly, past the point of maximum swirl.

(*c*) *Pressure distribution*

A comparison with the experimental pressure data is presented in figure 8. The data are obtained using the apparatus described in the previous section and the first three cases defined in table 1. Instead of seeding the flow for the purpose of PIV acquisition, a modified end cap is substituted with pressure taps located at non-dimensional radial intervals of 0.15, with the exception of two additional taps being placed near the wall at r=0.9 and 0.967. For simplicity, the experimental measurements are normalized by their values at the sidewall. As depicted in figure 8*a–c*, direct comparison with the shear stress model reflects substantial agreement in the outer region leading to the sidewall. As the data approaches the centreline, the model continues to mimic the general shape of the experimental distribution, although the measurements are seen to fall below the theoretical prediction. This trend may be attributed, in part, to the incompressible character of our approximation.

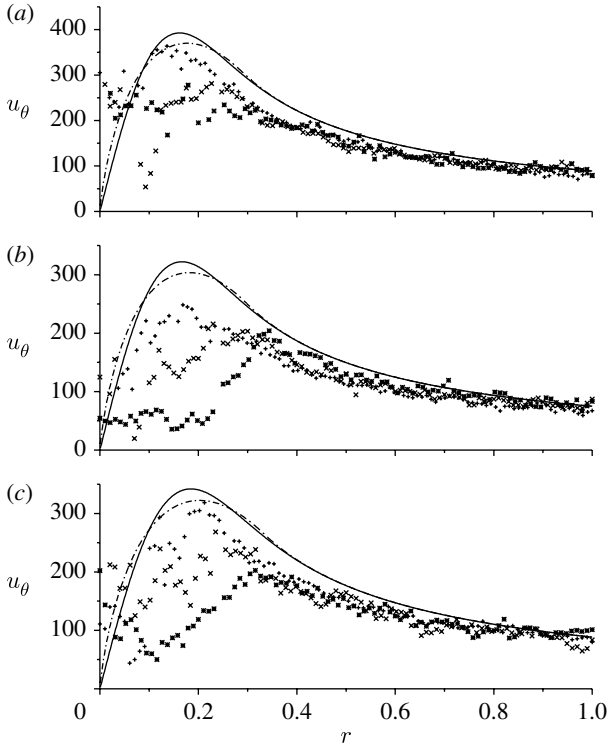

Figure 7. Comparison of the turbulent and modified laminar models with independent experimental data held in reserve for (*a*) V_t=29 150, (*b*) 27 650, and (*c*) 22 370. Plus, z/L=0.2; cross, z/L=0.5; star, z/L=0.7.

In two recent investigations by Majdalani (2007) and Maicke & Majdalani (2008), accounting for compressibility effects was shown to reduce the pressure values near the core of the chamber with successive increases in flow speed. This behaviour is further confirmed by Vatistas & Aboelkassem (2006) in a similar study of industrial cyclones.

(*d*) *Limitations*

Clearly, the models presented here are not unique as other reconciliatory schemes may be arrived at. The constant shear model swirl velocity overshoot and location must be thoroughly interrogated for validity via comparisons with experimental and robust computational predictions. Another model that may be pursued consists of calculating the matching radius such that the integrated shear stress associated with the constant shear approximation can be made to match the corresponding value predicted by the laminar core solution. At the outset, the surface areas under the $\tau_{r\theta}$ curves in figure 4*a* may be matched. Whether such a scheme could produce a more accurate approximation will remain a matter of conjecture until such time when the model is compared with a sufficiently large collection of experimental measurements and numerical predictions that are focused on parametric variations in the vortex Reynolds numbers. In similar fashion, the pressure distribution could be taken to be the

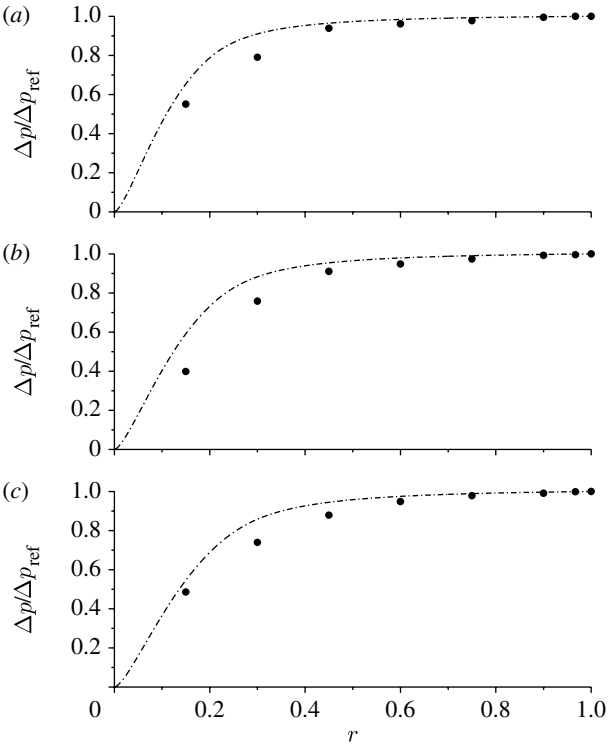

Figure 8. Comparison of the turbulent model with independent experimental data for the pressure given (*a*) V_t=47 150, (*b*) 36 540, and (*c*) 30 160. Dashed-dotted line, constant shear; filled circle, experiment.

target function for the model. As alluded to earlier, one may attempt to match pressure profiles such as those arising in figure 3 to the observed patterns. In short, the matching radius could be adjusted in a variety of ways to best model laboratory or numerical experiments.

Finally, it must be borne in mind that with the full onset of turbulence, the models presented here may retain their predictive value albeit at the expense of some loss in accuracy. Despite the presence of a nearly laminar core flow, the outer, annular motion may no longer remain irrotational. Turbulence has the ability to attract the surrounding irrotational fluid through frictional effects, specifically through entrainment (Kundu & Cohen 2002). While the source of entrainment may be attributed to viscous shear in laminar flows, it is mostly inertial in turbulent flows. In fact, the entrainment rate under turbulent conditions can far exceed any effects that are attributable to fluid friction. When the laminar core is affected by the turbulent outer flow, the resulting fluid is turbularized by the introduction of small viscous eddies that can be formed at the interface between the rotational and irrotational regions. In the bidirectional vortex chamber, the turbulent annulus can therefore entrain the core fluid to the extent of causing further departures from the newly established solutions. When these turbulent effects occur, we may expect to see higher swirl velocities from the peak region to the wall.

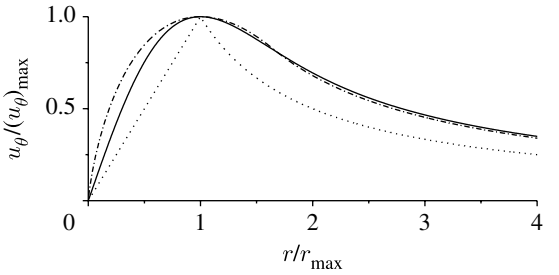

Figure 9. Optimally rescaled swirl velocity profiles for the laminar core model, constant shear stress model and Rankine's laminar model. Solid line, laminar core; dashed-dotted line, constant shear, dotted line, Rankine (1858).

(*e*) *Analogy with the Rankine model*

Figure 9 compares the shapes of the swirl velocity profiles for the laminar core model and constant shear solutions to Rankine's. In order to draw meaningful comparisons, both dependent and independent variables are renormalized. First, the radial coordinate is normalized by $r_{\max}$ such that the maximum velocity occurs at a value of unity. Second, each velocity is divided by its respective peak value in order to enforce uniformity of height. The unified normalization used here enables us to capture the basic similarities shared by these profiles. While the combined Rankine model consists of matching the forced vortex line with the outer vortex, both laminar core model and constant shear curves represent smooth blending of the inner and outer regions. In conformance with turbulent flow theory, a slight bulging of the constant shear velocity is observed (chained line) in relation to the laminar models (solid or broken lines).

(*f*) *Uniformly valid representation*

The constant shear model velocity described earlier appears to be a viable model for the bidirectional vortex core. However, it does not satisfy the no-slip condition at the wall. Instead, the tangential velocity at the sidewall remains equal to the circumferential injection speed, $\bar{u}_\theta(a,\bar{z}) = U$. This particular requirement coincides with the wall boundary condition that one may impose in a centrifuge where the cyclonic motion is induced by the rotating sidewall. The corresponding circular speed may be calculated to be $\omega_f = U/a$. A model that more adequately captures the behaviour of the bulk gas motion in the vortex combustion cold wall chamber is one that assumes a stationary sidewall. The wall-bounded counterpart of the present solution may hence be obtained by combining the constant shear-based core approximation with an outer, annular profile that observes the velocity adherence condition. Such profile may be directly obtained from the work of Vyas & Majdalani (2006*b*) for the tangential velocity. Furthermore, the axial and radial velocity components may be asymptotically extended to account for the confining wall. As shown by Batterson & Majdalani (2007) a wall-bounded solution may be arrived at using the tools of matched-asymptotic expansions. A uniformly valid wall-to-wall approximation may be constructed in which the three components of the velocity are given by

$$\left\{\begin{array}{l} u_r = -\dfrac{\kappa}{r}\sin(\pi r^2)\left\{1-\exp\left[-\dfrac{1}{2}\left(\dfrac{1}{6}\pi^2-1\right)V(1-r^2)\right]\right\}, \\ u_z = 2\pi\kappa z\cos(\pi r^2)\left\{1-\exp\left[-\dfrac{1}{4}\left(\dfrac{1}{6}\pi^2-1\right)V(1-r^2)\right]\right\}, \\ u_\theta = \begin{cases} rVX_0^{-2}\ell_t[1-2\ln(r\sqrt{V\ell_t}/X_0)]; & r \le X_0/\sqrt{V\ell_t}, \\ \dfrac{1}{r}\left\{1-\exp\left[-\dfrac{1}{4}\left(\dfrac{1}{6}\pi^2-1\right)V(1-r^2)\right]\right\}; & r > X_0/\sqrt{V\ell_t}, \end{cases} \end{array}\right. \tag{4.14}$$

where $X_0 \backsimeq 50$. Equation (4.14) is a modified form of the constant shear approximation that is rectified so as to satisfy the no slip condition. It closely resembles (3.5) and (2.8) except near the sidewall.

5. Conclusions

In this paper, two basic formulations for the swirl velocity of the bidirectional vortex under high speed conditions are presented and discussed. A constant shear stress model is first employed to extract the velocity near the core that is then matched to an outer solution that is mainly irrotational. The ensuing approximation exhibits one degree of freedom that enables us to anchor our solution for a given flow pattern. This predictive feature is set by relating the matching radius of the constant shear stress model to the vortex Reynolds number arising in a given application, $X \backsimeq X_0/\sqrt{V_t}$. Since the matching point delimits the inner zone, where the shear stress may be taken to be uniform, linking this radius to the vortex Reynolds number enables us to control the thickness of the core region along with the maximum speed that the tangential velocity may reach. The matching process grants our constant shear stress model the ability to conform to a nearly arbitrary swirl pattern over a practical range of Reynolds numbers. Based on available laboratory measurements and least-squares analyses, the correlation constant $X_0 \backsimeq 50$ is obtained and shown to be nearly invariant with the vortex Reynolds number. Compared with the modified laminar core model, the experimentally anchored constant shear solution displays a broader velocity profile that is characteristic of high speed flows. However, further extensions to this solution, such as compressible corrections, have to be piecewise as well. The modified laminar core approach employs a modified vortex Reynolds number, $V = V_t/\ell_t$, resting on the concept of an enhanced eddy viscosity ratio $\ell_t \backsimeq 152$. Being the by-product of matched-asymptotic expansions and the Navier–Stokes equations, the modified laminar core solution remains continuous and uniformly valid across the chamber cross-section. At first glance, it may be surprising that a constant shear stress condition in the core could nearly duplicate the behaviour of a laminar model derived from the Navier–Stokes equations. Upon further scrutiny, however, it may be realized that a large body of experimental evidence supports the notion that vortices display an approximately constant angular velocity core with low turbulence levels to the extent that they may be treated as laminar. Turbulent

diffusion is therefore limited to a narrow area that surrounds the laminar zone. Outside the turbulent zone, an inviscid flow approximation may be assumed as in the case of a potential outer vortex. Thus, given that a laminar core with constant angular velocity is accompanied by nearly constant shear, its ability to reproduce similar features to those associated with the constant shear stress approximation is confirmatory. Hence, in addition to the core modelling choices debated here, the laminar model for the bidirectional vortex is substantially improved through the use of an empirically based turbulent eddy viscosity. It is hoped that future experiments and numerical simulations will be correlated versus the vortex Reynolds number, thus helping to validate and refine the present models.

This project was funded by the National Science Foundation through grant No. CMMI-0353518, Dr Eduardo A. Misawa, Program Director. The authors are grateful to both Dr Martin J. Chiaverini from Orbital Technologies Corporation and Dr Mark H. Anderson from the University of Wisconsin for providing the experimental data at high vortex Reynolds numbers.

References

Alekseenko, S. V., Kuibin, P. A., Okulov, V. L. & Shtork, S. I. 1999 Helical vortices in swirl flow. *J. Fluid Mech.* **382**, 195–243. (doi:10.1017/S0022112098003772)

Batterson, J. W. & Majdalani, J. 2007 On the boundary layers of the bidirectional vortex. In *AIAA Paper 2007–4123*. Reston, VA: AIAA.

Bloor, M. I. G. & Ingham, D. B. 1987 The flow in industrial cyclones. *J. Fluid Mech.* **178**, 507–519. (doi:10.1017/S0022112087001344)

Chiaverini, M. J., Malecki, M. J., Sauer, J. A., Knuth, W. H. & Majdalani, J. 2003 Vortex thrust chamber testing and analysis for O2-H2 propulsion applications. In *AIAA Paper 2003–4473*. Reston, VA: AIAA.

Derksen, J. J. 2005 Simulations of confined turbulent vortex flow. *Comput. Fluids* **34**, 301. (doi:10.1016/j.compfluid.2004.06.001)

Derksen, J. J. & Van den Akker, H. E. A. 2000 Simulation of vortex core precession in a reverse flow cyclone. *AICHE J.* **46**, 1317–1331. (doi:10.1002/aic.690460706)

Escudier, M. P., Bornstein, J. & Zehnder, N. 1980 Observations and LDA measurements of confined turbulent vortex flow. *J. Fluid Mech.* **98**, 49–63. (doi:10.1017/S0022112080000031)

Escudier, M. P., Bornstein, J. & Maxworthy, T. 1982 The dynamics of confined vortices. *Proc. R. Soc. A* **382**, 335–360. (doi:10.1098/rspa.1982.0105)

Faler, J. H. & Leibovich, S. 1978 An experimental map of the internal structure of a vortex breakdown. *J. Fluid Mech.* **86**, 313–335. (doi:10.1017/S0022112078001159)

Fang, D., Majdalani, J. & Chiaverini, M. J. 2003 Simulation of the cold-wall swirl driven combustion chamber. In *AIAA Paper 2003–5055*. Reston, VA: AIAA.

Gupta, A. K., Lilley, D. G. & Syred, N. 1984 *Swirl flows*. London, UK: Abacus.

Hoekstra, A. J., Van Vliet, E., Derksen, J. J. & Van den Akker, H. E. A. 1998 Vortex core precession in a gas cyclone. In *Advances in turbulence*, vol. VII (ed. U. Frisch), pp. 289–292. Dordrecht, The Netherlands: Kluwer.

Hu, L. Y., Zhou, L. X., Zhang, J. & Shi, M. X. 2005 Studies of strongly swirling flows in the full space of a volute cyclone separator. *AICHE J.* **51**, 740–749. (doi:10.1002/aic.10354)

Königl, A. 1986 Stellar and galactic jets: theoretical issues. *Can. J. Phys.* **64**, 362–368.

Kundu, P. K. & Cohen, I. M. 2002 *Fluid mechanics*, 2nd edn. San Diego, CA: Academic Press.

Leibovich, S. 1978 The structure of vortex breakdown. *Annu. Rev. Fluid Mech.* **10**, 221–246. (doi:10.1146/annurev.fl.10.010178.001253)

Maicke, B. A. & Majdalani, J. 2008 On the rotational compressible Taylor flow in injection-driven porous chambers. *J. Fluid Mech.* **603**, 391–411. (doi:10.1017/S0022112008001122)

Majdalani, J. 2007 On steady rotational high speed flows: the compressible Taylor–Culick profile. *Proc. R. Soc. A* **463**, 131–162. (doi:10.1098/rspa.2006.1755)

Majdalani, J. & Rienstra, S. W. 2007 On the bidirectional vortex and other similarity solutions in spherical coordinates. *Z. Angew. Math. Phys.* **58**, 289–308. (doi:10.1007/s00033-006-5058-y)

Murray, A. L., Gudgen, A. J., Chiaverini, M. J., Sauer, J. A. & Knuth, W. H. 2004 Numerical code development for simulating gel propellant combustion processes. JANNAF Paper (unclassified).

Ogawa, A. 1984 Estimation of the collection efficiencies of the three types of the cyclone dust collectors from the standpoint of the flow pattern in the cylindrical cyclone dust collectors. *Bull. JSME* **27**, 64–69.

Penner, S. S. 1972 Elementary considerations of the fluid mechanics of tornadoes and hurricanes. *Acta Ast.* **17**, 351–362.

Rankine, W. J. M. 1858 *A manual of applied mechanics*, 9th edn. London, UK: C. Griffin and Co.

Rom, C. 2006 *Flow field and near nozzle fuel spray characterizations for a cold flowing vortex engine*. Madison, WI: University of Wisconsin-Madison.

Rom, C. J., Anderson, M. H. & Chiaverini, M. J. 2004 Cold flow analysis of a vortex chamber engine for gelled propellant combustor applications. In *AIAA Paper 2004–3359*. Reston, VA: AIAA.

Szeri, A. & Holmes, P. 1988 Nonlinear stability of axisymmetric swirling flows. *Phil. Trans. R. Soc. Lond. A* **326**, 327–354. (doi:10.1098/rsta.1988.0091)

Tennekes, H. & Lumley, J. L. 1976 *A first course in turbulence*. Cambridge, MA: MIT Press.

ter Linden, A. J. 1949 Investigations into cyclone dust collectors. *Proc. Inst. Mech. Eng.* **160**, 233–251. (doi:10.1243/PIME_PROC_1949_160_025_02)

Townsend, A. A. 1976 *The structure of turbulent shear flow*. Cambridge, UK: Cambridge University Press.

Trapp, R. J. 2000 A clarification of vortex breakdown and tornadogenesis. *Mon. Weather Rev.* **128**, 888–895. (doi:10.1175/1520-0493(2000)128<0888:ACOVBA>2.0.CO;2)

Vatistas, G. H. 2006 Simple model for turbulent tip vorticies. *J. Aircraft* **43**, 1577–1578. (doi:10.2514/1.22477)

Vatistas, G. & Aboelkassem, Y. 2006 Extension of the incompressible $n=2$ vortex into compressible. *AIAA J.* **44**, 1912–1915. (doi:10.2514/1.18511)

Vatistas, G. H., Lin, S. & Kwok, C. K. 1986 Theoretical and experimental studies on vortex chamber flows. *AIAA J.* **24**, 635–642. (doi:10.2514/3.9319)

Vatistas, G. H., Jawarneh, A. M. & Hong, H. 2005 Flow characteristics in a vortex chamber. *Can. J. Chem. Eng.* **83**, 425–436.

Vyas, A. B. & Majdalani, J. 2006*a* Exact solution of the bidirectional vortex. *AIAA J.* **44**, 2208–2216. (doi:10.2514/1.14872)

Vyas, A. B. & Majdalani, J. 2006*b* Characterization of the tangential boundary layers in the bidirectional vortex thrust chamber. In *AIAA Paper 2006–4888*. Reston, VA: AIAA.

Vyas, A. B., Majdalani, J. & Chiaverini, M. J. 2003 The bidirectional vortex. Part 2: viscous core corrections. In *AIAA Paper 2003–5053*. Reston, VA: AIAA.

White, F. M. 1991 *Viscous fluid flow*. New York, NY: McGraw-Hill.